

Article

Boosting Oxygen Electrocatalysis by Combining Iron Nanoparticles with Single Atoms

Bowen Liu , Sihong Wang, Fang Song * and Qinglei Liu *

State Key Laboratory of Metal Matrix Composites, School of Materials Science and Engineering, Shanghai Jiao Tong University, Shanghai 200240, China; liu-bowen@sjtu.edu.cn (B.L.); wangsihong@sjtu.edu.cn (S.W.)

* Correspondence: songfang@sjtu.edu.cn (F.S.); liuqinglei@sjtu.edu.cn (Q.L.)

Abstract: The development of high-performance non-noble metal-based oxygen electrocatalysts is crucial for the practical application of zinc–air batteries. Most of them suffer from low intrinsic activity and poor stability, failing to meet the needs of practical applications. Here, we report an efficient and durable bifunctional oxygen electrocatalyst of Fe@Fe-SAC composite (SAC stands for single atoms on carbon). A facile and ease-to-scale-up process synthesizes it. Fe single-atom and Fe nanoparticles are anchored on nitrogen-doped porous carbon, with the latter encapsulated by the graphitic shell. It exhibits appealing activity and durability in a basic electrolyte, requiring a half-wave potential of 0.805 V for oxygen reduction reaction (ORR) and an overpotential of only 348 mV to deliver a current density of 10 mA cm⁻² for oxygen evolution reaction (OER). Both activities are comparable to the corresponding benchmarking electrocatalyst of Pt/C for ORR and IrO₂ for OER. The superior activities are attributed to the strong electronic interaction between metal single-atom and nanoparticles. The favorable stability is ascribed to the physical encapsulation of carbon coatings on nanoparticles. This work presents a feasible scheme for designing and large-scale preparation of high-performance non-noble metal-based bifunctional oxygen electrocatalysts.

Keywords: metal nanoparticle; single atom; oxygen reduction reaction; oxygen evolution reaction



Citation: Liu, B.; Wang, S.; Song, F.; Liu, Q. Boosting Oxygen Electrocatalysis by Combining Iron Nanoparticles with Single Atoms. *Catalysts* **2022**, *12*, 585. <https://doi.org/10.3390/catal12060585>

Academic Editors: Lichen Bai and Jun Gu

Received: 30 April 2022

Accepted: 25 May 2022

Published: 27 May 2022

Publisher's Note: MDPI stays neutral with regard to jurisdictional claims in published maps and institutional affiliations.



Copyright: © 2022 by the authors. Licensee MDPI, Basel, Switzerland. This article is an open access article distributed under the terms and conditions of the Creative Commons Attribution (CC BY) license (<https://creativecommons.org/licenses/by/4.0/>).

1. Introduction

As the global energy demand increases, there is an urgent need to develop a clean and renewable energy system to replace fossil fuels to solve climate warming and energy depletion [1,2]. Rechargeable Zn–air batteries (ZABs) are among the most promising energy conversion and storage devices because of their high theoretical energy density, cost-effectiveness, and environmental friendliness [3–5]. High-performance catalysts are required to accelerate the oxygen reduction and oxygen evolution reactions (ORR and OER) occurring at the air cathode, thereby improving the performance and efficiency of ZABs [6,7]. Noble metal catalysts such as Pt and IrO₂ are commonly used to catalyze ORR and OER; however, they are restricted by the high cost and scarcity [8,9]. Developing efficient, durable, and inexpensive electrocatalysts to replace noble-metal-based materials is the key to promoting the practical application of ZABs.

Transition metal nanoparticles (Fe, Co, Ni, etc.) are among the most promising non-noble metal-based oxygen electrocatalysts [10,11]. Fe nanoparticles supported by nitrogen-doped carbon are competitive ORR electrocatalysts [12,13]. Unfortunately, they show limited OER activity and deactivate fast in the long-term OER electrocatalysis [14,15]. Fe single-atom catalyst is an emerging candidate with attractive ORR and OER activities and extremely high atom utilization efficiency [16–18]. Single-atom Fe–N–C catalyst has the theoretically most increased activity for consecutive four-electron transfer ORR, but still has an overpotential of ≈0.48 V [19]. It is promising to combine single atoms with transition metal nanoparticles, as it can effectively tune the electronic structures

of carbon/metal composites [20–22] and regulate the adsorption behavior of ORR/OER intermediates, thus offering more possibilities to enhance the electrocatalytic performance of transition metal-based catalysts. Among them, metal–organic frameworks (MOF) have been extensively explored to produce transition metal-based hybrid catalysts [21–24]. High-temperature pyrolysis is usually indispensable for carbonization. The temperature could be higher than the boiling point of Zn (907 °C) for the purpose to evaporate Zn in the MOF precursor. Such a high temperature causes nanoparticles growth to a large size, which is detrimental to catalytic activity. For instance, the Fe nanoparticles in Fe_{NP}@Fe-N-C [21] and Co nanoparticles in the Co-NCS-2 [23] were up to 20 nm. Besides, the resultant catalysts typically had a relatively low nanoparticle loading and were more exposed to electrolytes directly, suffering from inferior OER catalysis and durability [23].

Furthermore, the uniform dispersion of transition metal nanoparticles/single atoms is essential for high-performance catalysts. Nitrogen-doped carbon is often used to support metal nanoparticles [25–27]. Heteroatom-doped carbon can act as an electron donor or acceptor, allowing charge transfer from or to transition metals [28]. In addition, porous carbon has a large surface area, which facilitates the exposure of active sites and mass transport [29]. However, uniform and dense distribution of nanoparticles or single atoms are usually fabricated by sophisticated and complex processes, which limit their large-scale production. In addition, hierarchically porous carbon materials favorable for mass transformation are still difficult to obtain.

Here, we report an iron-based composite of Fe@Fe-SAC (SAC stands for single atoms on carbon) for the efficient electrocatalytic oxygen reduction and oxygen evolution reaction. Fe@Fe-SAC composites were synthesized via a simple two-step method using sodium alginate as a carbon precursor. Both iron nanoparticles and single iron atoms were anchored on nitrogen-doped porous carbon in the annealing process. It shows appealing catalytic activities for both electrocatalytic oxygen reduction reaction and oxygen evolution reaction. Spectroscopic and electrochemical analyses were done to understand the origin of the superior activity. This work presents a feasible scheme for the large-scale preparation of high-performance non-noble metal electrocatalysts for ORR and OER.

2. Results and Discussion

2.1. Synthesis and Structural Characterizations

Fe@Fe-SAC was synthesized through a simple, reproducible, and easy-to-scale-up method. In a typical process, the aqueous sodium alginate solution was added to resolution of iron ions. The hydrophilic groups (e.g., –COOH, –OH) of the guluronic acid segment of sodium alginate can chelate with multivalent metal cations to form a stable microcrystalline area called “egg-box” structures [30]. The formed hydrogel was collected from the solution, and freeze-dried to obtain aerogel fibers. Finally, the aerogel fibers were annealed in an ammonia atmosphere for carbonization, crystallization, and producing single atoms. The “egg-box” structures disperse metal ions homogeneously and further stabilize the composites, reducing the agglomeration of metal atoms in pyrolysis.

The powder X-ray diffraction pattern of Fe@Fe-SAC (Figure 1a) shows sharp diffraction peaks at 44.7°, 65.0°, and 82.3°, corresponding to the (110), (200), and (211) crystal planes of body-centered cubic structures of metallic Fe (JSPDF No. 06-0696). The average particle size of Fe nanoparticles in Fe@Fe-SAC is calculated to be around 8 nm by the Debye-Scherrer equation. Raman spectrum was used to characterize the graphitization degree of Fe@Fe-SAC (Figure 1b). The I_G/I_D value is ≈0.8, indicating good conductivity of Fe@Fe-SAC. Nitrogen adsorption–desorption measurement (Figure 1c) shows the Fe@Fe-SAC has a Brunauer–Emmett–Teller (BET) surface area of 283 m² g^{−1}, which is larger than that of commercial Pt/C (207 m² g^{−1}). The pore size distribution of Fe@Fe-SAC ranges from 4 to 7 nm, while the pore size of Pt/C peaks at 1 nm (Figure 1d). The large surface area and abundant pores allow active sites to participate in the catalytic reaction.

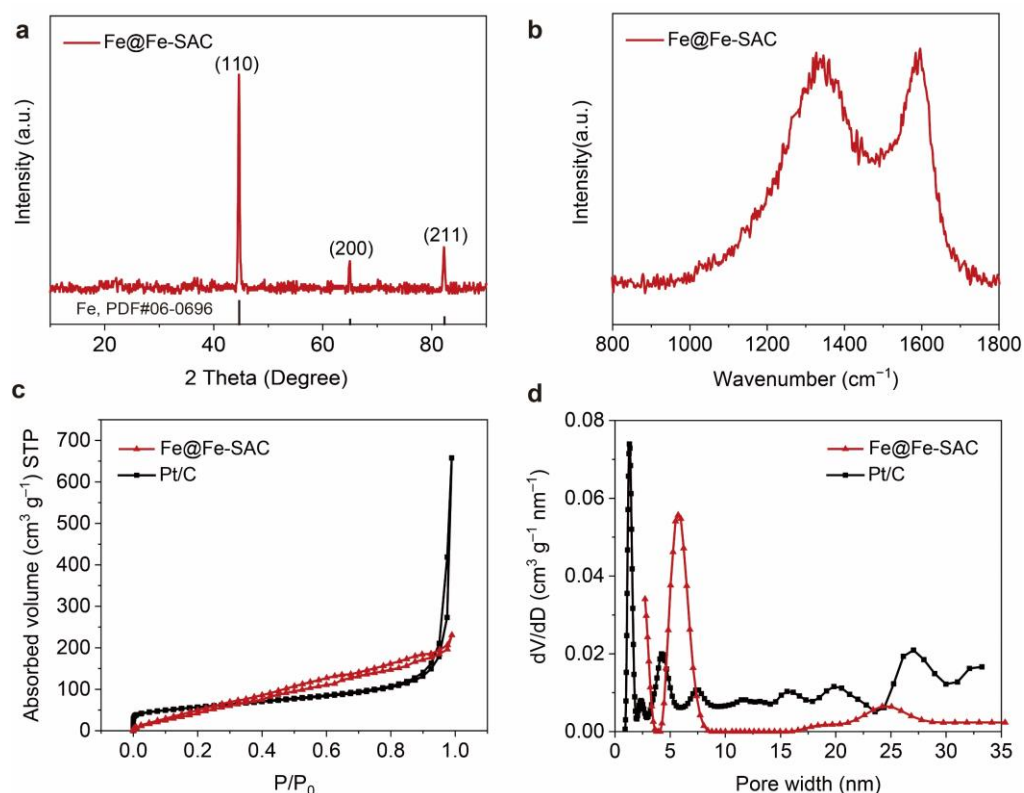


Figure 1. (a) X-ray diffraction pattern, (b) Raman spectra, (c) Nitrogen adsorption–desorption isotherm, and (d) pore size distribution of Fe@Fe-SAC.

The scanning electron microscopic (SEM) image shows that Fe@Fe-SAC has a fibrous carbon network (Figure 2a). The diameter of the fibers is ≈ 20 nm. The transmission electron microscopic (TEM) image (Figure 2b) shows well-dispersed nanoparticles of ≈ 7 nm inlay carbon fibers. The nanoparticles are coated with 3–5 layers of nanoporous carbon, as revealed by the high-resolution TEM (HRTEM) image (Figure 2c). The spherical aberration-corrected TEM shows that isolated bright single atoms are densely distributed on the carbon matrix (Figure 2d). It also manifests a clear lattice fringe of nanoparticles, measured to be 2.03 Å, and corresponds to the (110) interplanar spacings of Fe crystals. This result confirms the formation of Fe nanoparticles and single atoms on carbon fibers. The elemental mapping result (Figure 2e) ensures that Fe nanoparticles are loaded on the N-doped carbon substrate. Elemental analysis on carbon substrate confirms the single atoms are Fe (Figure 2f).

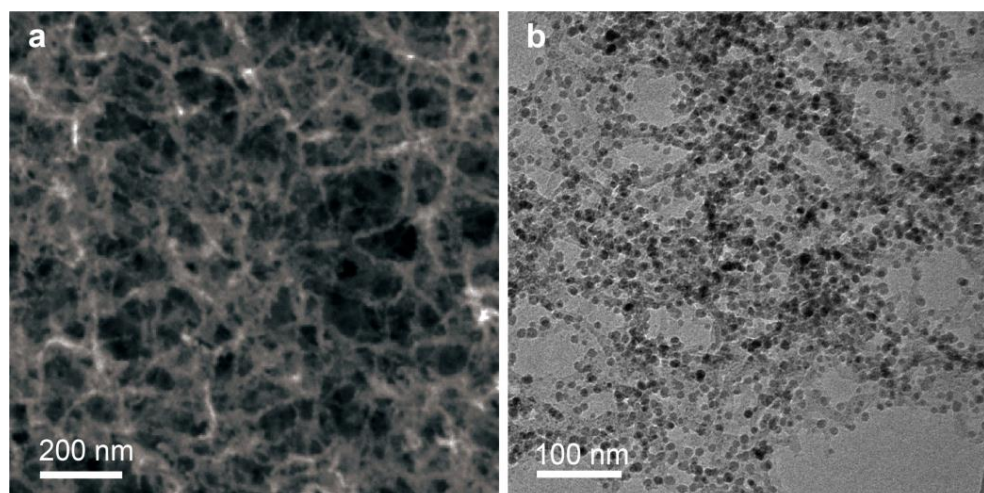


Figure 2. Cont.

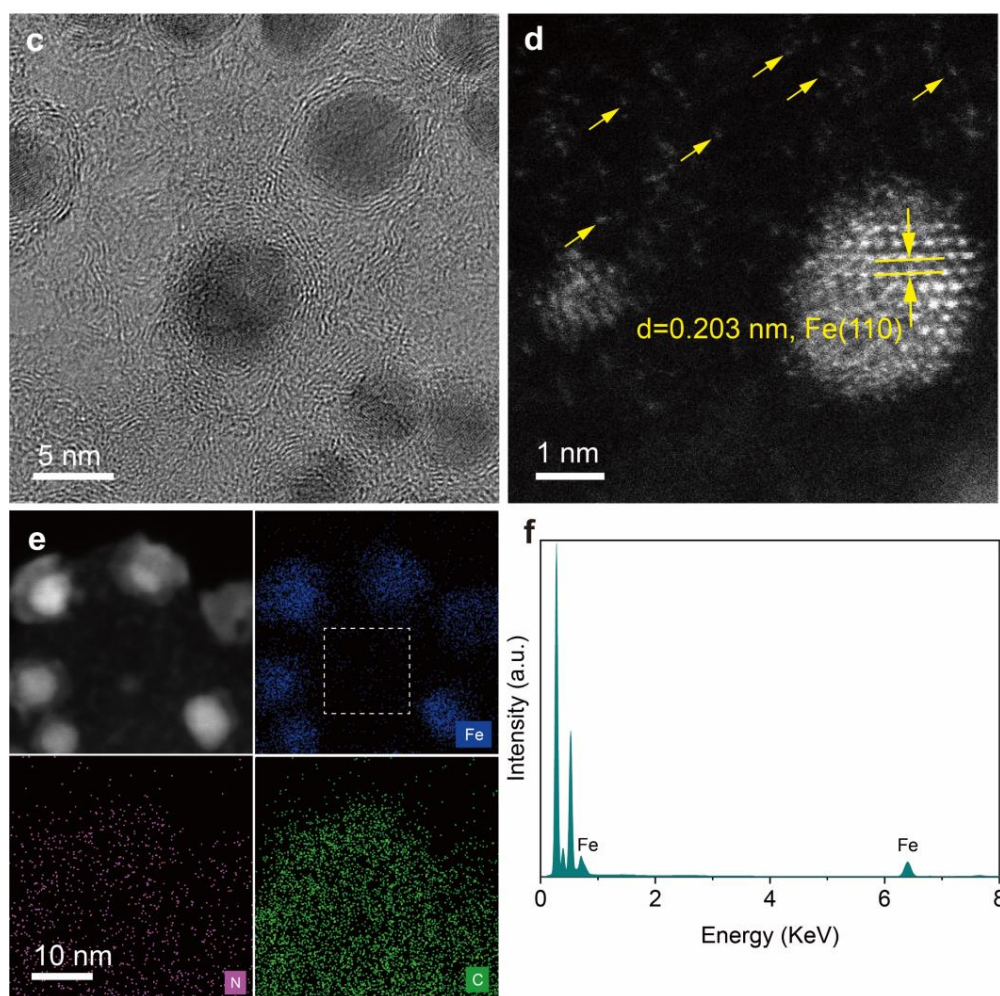


Figure 2. Microstructural characterizations of Fe@Fe-SAC. (a) SEM image, (b) TEM image, (c) HRTEM image, and (d) atomic resolution HAADF-STEM image of Fe@Fe-SAC (a portion of single atoms are indicated by yellow arrows). (e) HAADF-STEM and corresponding elemental mapping images. (f) EDS of the carbon substrate (marked by a square in e).

X-ray photoelectron spectroscopy (XPS) was used to characterize the electronic structure of Fe@Fe-SAC. Fe single atoms on carbon (Fe-SAC) were obtained by dissolving Fe nanoparticles in Fe@Fe-SAC with hydrochloric acid, and it was selected as the reference. High-resolution spectra of Fe 2p are shown in Figure 3a. The Fe 2p XPS spectrum of Fe@Fe-SAC can be deconvoluted into six peaks, namely metallic Fe(0) peaks (located at 707.28 eV and 720.48 eV), Fe²⁺ (located at 710.22 eV and 723.42 eV), Fe³⁺ (located at 713.20 eV and 726.40 eV), and satellite peaks. The Fe²⁺ and Fe³⁺ in Fe@Fe-SAC correspond to Fe single atoms and FeO_x on the surface of Fe nanoparticles (oxidized by air) [20]. The Fe 2p spectrum of Fe-SAC has no peaks of metallic Fe(0), confirming the complete dissolution of Fe nanoparticles. Notably, the Fe 2p peak of Fe@Fe-SAC shifts to lower binding energy by about 0.56 eV than that of Fe-SAC. This result indicates partial electron transfer between metal nanoparticles and single metal atoms in Fe@Fe-SAC. The O 1s XPS spectrum of Fe@Fe-SAC (Figure 3b) can be deconvoluted into three peaks, corresponding to Fe–O (530.10 eV), C=O (531.88 eV), and adsorbed oxygen (533.70 eV) with the atomic ratio of 0.22:0.52:0.26. The overall atomic percentage of oxygen is 7.4%. The absence of Fe–O peak agrees well with the entire dissolution of Fe nanoparticles in Fe-SAC. The N 1s spectrum of Fe@Fe-SAC (Figure 3c) can be deconvoluted into five peaks: pyridinic N (398.25 eV), Fe–N_x (399.21 eV), pyrrolic N (400.30 eV), graphitic N (401.10 eV), and oxidized N (403.33 eV), having an atomic ratio of 0.31:0.14:0.17:0.19:0.19. The presence of Fe–N_x peaks in the N 1s

XPS spectra verifies the formation of Fe single atoms. Based on the XPS result, the overall atomic percentage of N is 5.41% in Fe@Fe-SAC. Moreover, C=N peaks in the C 1s XPS spectra demonstrate that N is successfully doped into the carbon matrix (Figure 3d).

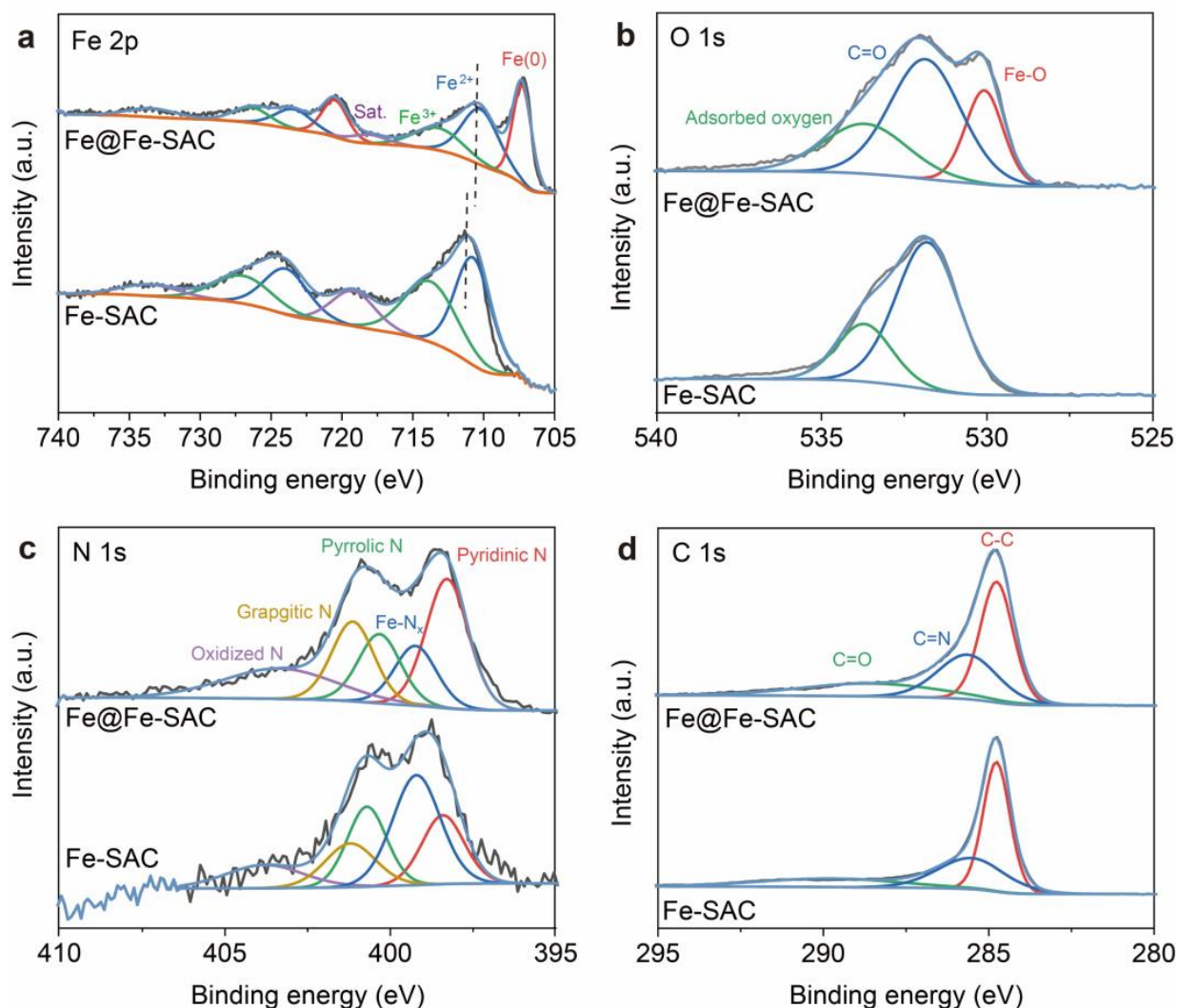


Figure 3. XPS spectra of Fe@Fe-SAC and Fe-SAC. (a) Fe 2p XPS spectra, (b) O 1s XPS spectra, (c) N 1s XPS spectra, and (d) C 1s XPS spectra.

2.2. Electrocatalytic ORR and OER Performance

The ORR performance of Fe@Fe-SAC was first investigated in an O₂-saturated 0.1 M KOH electrolyte by a rotating disk electrode (RDE) method. The current density was normalized by electrode geometric area (The electrochemical specific surface area is not used here, as it is to date challenging to obtain for non-noble metal catalysts). The cyclic voltammetry curves show a more positive cathodic peak in Fe@Fe-SAC (Figure 4a), suggesting a higher activity for the oxygen reduction reaction. Linear sweep voltammetry (LSV) curves (Figure 4b) show that Fe@Fe-SAC has a half-wave potential ($E_{1/2}$) of 0.805 V versus reversible hydrogen electrode (RHE), surpassing Fe-SAC (0.749 V), and comparable to commercial Pt/C (0.848 V). The kinetic current densities were calculated from the Koutechy-Levich equation to evaluate the intrinsic catalytic activities. Fe@Fe-SAC has a high kinetic current density of 8.25 mA cm⁻² at 0.8 V vs. RHE (Figure 4c). It has a Tafel slope of 79.65 mV dec⁻¹, close to that of commercial Pt/C (79.15 mV dec⁻¹), while it is much smaller than Fe-SAC (94.53 mV dec⁻¹, Figure 4d). This suggests that Fe@Fe-SAC has faster kinetics than Fe-SAC, likely due to the strong electronic interaction between nanoparticles and single atoms. Rotating ring-disk electrode (RRDE) measurement was conducted to get

the electron transfer number (n) and calculate the peroxide yield ($\text{H}_2\text{O}_2\%$). Fe@Fe-SAC shows a near 4-electron ORR pathway, similar to commercial Pt/C. The H_2O_2 yields of Fe@Fe-SAC are below 17% at the potential range of 0.2–0.8 V versus RHE (Figure 4e). In contrast, Fe-SAC has an electron transfer number of ≈ 3.4 and a higher H_2O_2 yield of 31.5%. This indicates that Fe@Fe-SAC has better selectivity for electrocatalytic oxygen reduce to water. In addition to catalytic activity, stability is also an important indicator for practical applications. The stability of Fe@Fe-SAC was evaluated by performing the accelerating durability tests (ADT). The half-wave potential of Fe@Fe-SAC is negatively shifted by only 14 mV in 10,000 potential cycles (Figure 4f), demonstrating favorable stability in a basic electrolyte.

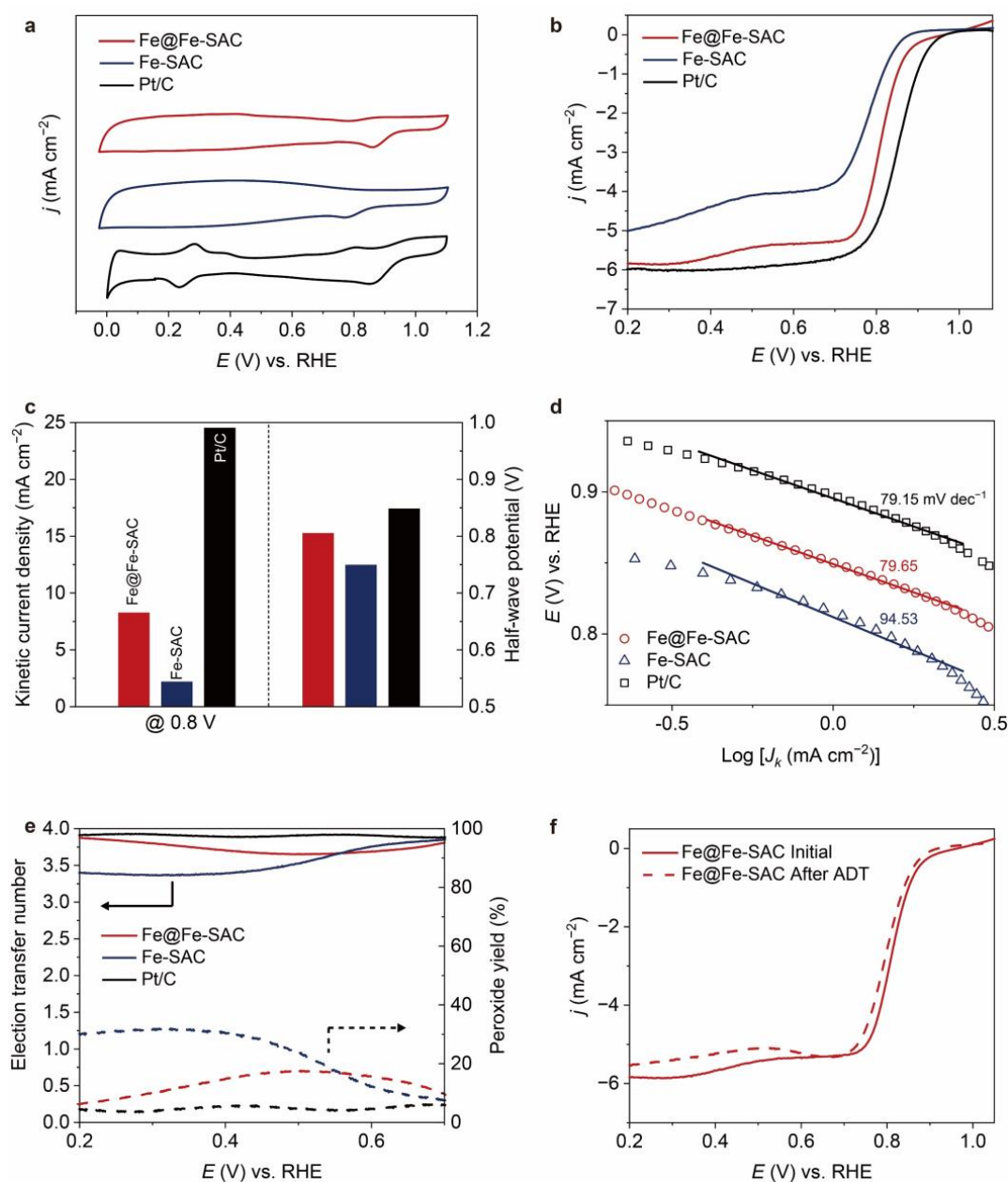


Figure 4. Electrocatalytic ORR performance of Fe@Fe-SAC. (a) Cyclic voltammograms recorded in an O_2 -saturated 0.1 M KOH solution. (b) Linear sweep voltammograms recorded in an O_2 -saturated 0.1 M KOH solution. (c) Kinetic current density and half-wave potential. (d) Tafel plots derived from ORR polarization curves. (e) Electron transfer number and peroxide yield plots. (f) LSV evolutions.

To reveal the reason for the good stability of Fe@Fe-SAC, TEM was performed to characterize samples after ADT. Fe@Fe-SAC retains the morphology (Figure 5a). The metal nanoparticles are still well dispersed on the carbon matrix, with few perceptible agglomerations and no particle size changes (Figure 5a,b). The lattice fringe suggests the Fe nanoparticles retain the metallic nature in Fe@Fe-SAC (Figure 5c). In addition, the carbon layer on the particle surface remains intact (Figure 5b), indicating the good stability of Fe–N–C single atoms. The good stability of Fe@Fe-SAC should be attributed to the carbon shell encapsulation, which alleviates the corrosion of the Fe nanoparticles under ORR potentials.

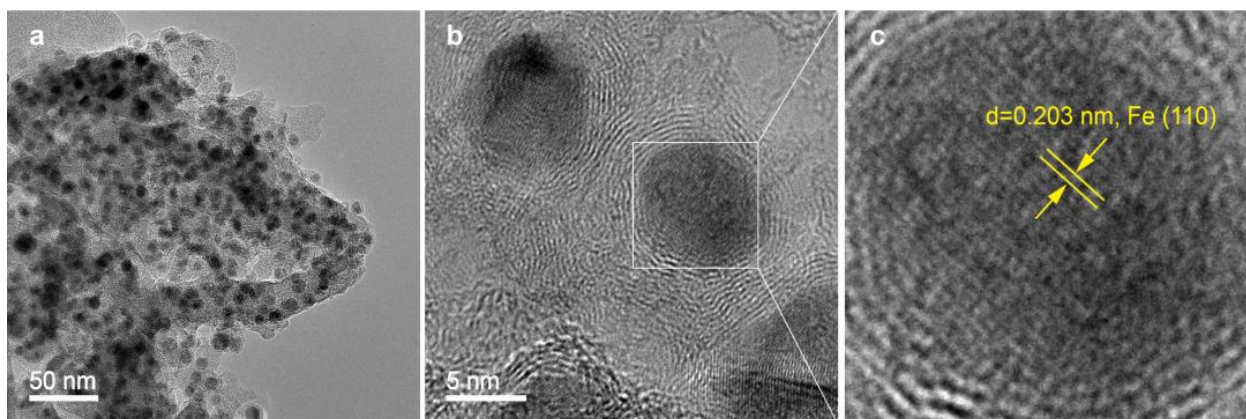


Figure 5. Microstructural characterizations of Fe@Fe-SAC after ADT. (a) TEM image and (b,c) HRTEM image of Fe@Fe-SAC after ADT.

Aside from good ORR performances, Fe@Fe-SAC also exhibits superior electrocatalytic activity toward OER. It was evaluated in a 1 M KOH electrolyte by a three-electrode system. Figure 6a shows the OER polarization curves of Fe@Fe-SAC, Fe foil, FeOOH, and commercial IrO₂. Fe@Fe-SAC exhibits the best catalytic activity among Fe-based catalysts (Figure 6b). The overpotential is only 0.348 V at a current density of 10 mA cm⁻², 125–230 mV lower than the other two Fe-based materials (FeOOH: 0.578 V, Fe foil: 0.473 V). Notably, it is comparable to that of IrO₂. The Tafel slope analysis suggests the appealing catalytic activity (Figure 6c). Fe@Fe-SAC exhibits a Tafel slope of 55.61 mV dec⁻¹, close to that of Fe foil (52.11 mV dec⁻¹) but much lower than FeOOH (188.9 mV dec⁻¹). Based on the above analysis, we conclude that Fe nanoparticles in Fe@Fe-SAC should predominantly contribute to the OER activity, where Fe single atoms may act as a promoter to regulate the electronic structures (as revealed by the XPS spectra aforementioned). The long-term catalytic stability of Fe@Fe-SAC was evaluated by a chronoamperometric method. At a constant potential of 1.6 V versus RHE, the current dropped by only 11% within 4 h, showing good stability in a basic electrolyte (Figure 6d).

As shown by the XRD pattern (Figure 1a) and HRTEM image (Figure 2d), the Fe nanoparticles expose the (110) crystal planes predominantly. A previous study has shown that electrons are prone to transport from (110) planes of Fe nanoparticles to the encapsulated carbon layer, enhancing catalytic activity [31]. Our Fe@Fe-SAC composites may similarly proceed the catalysis. The XPS spectra in Figure 3a suggest that the carbon layers decorated with single atoms have strong electronic interaction with nanoparticles. The synergistic effect may regulate the electronic structure for optimized adsorption of reaction intermediates, thereby enhancing the catalytic activity of ORR and OER. In addition, the porous carbon fiber matrix might improve the accessibility of active sites and facilitate the mass transport of electrolytes and reactants.

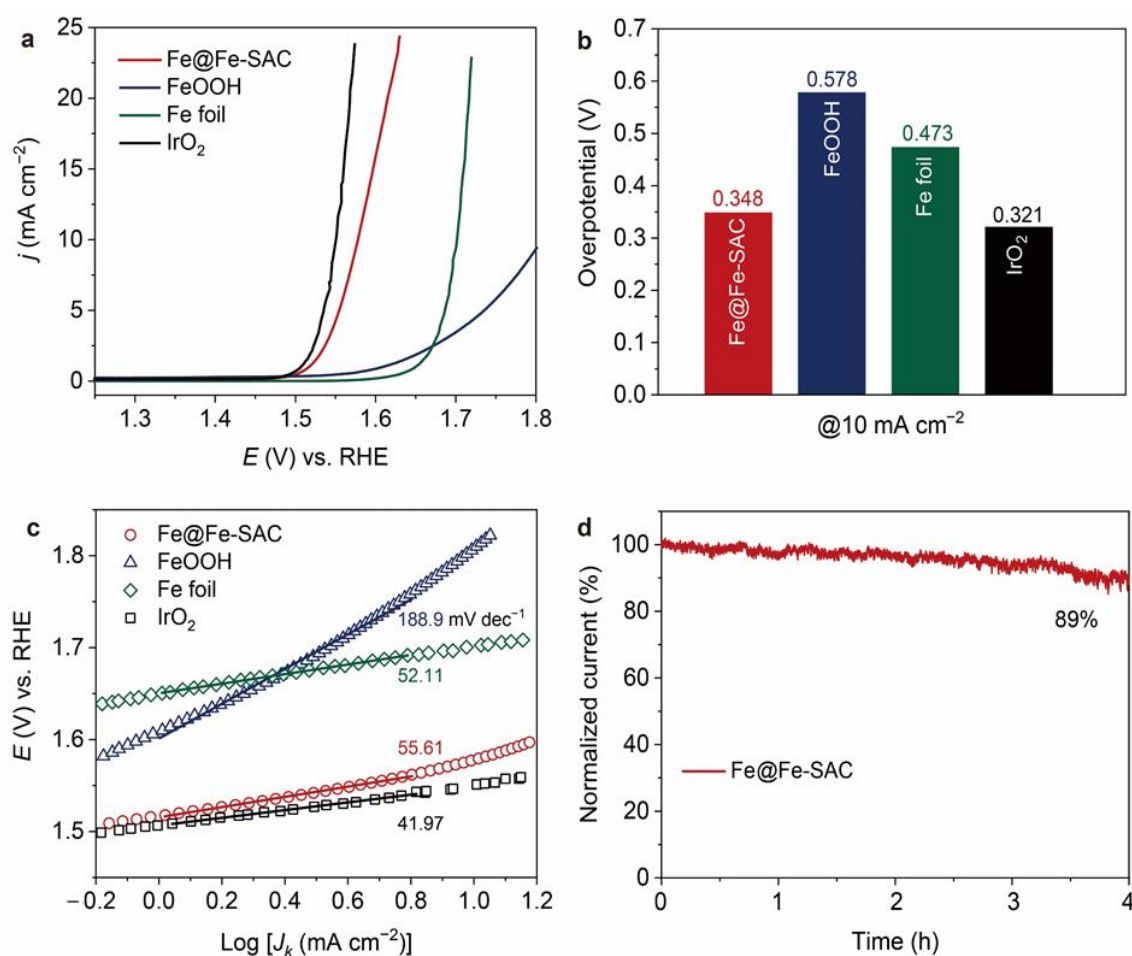


Figure 6. Electrocatalytic OER performance of Fe@Fe-SAC. (a) OER polarization curves recorded in an O₂-saturated 1 M KOH solution. (b) Overpotentials at a current density of 10 mA cm⁻². (c) Tafel plots derived from OER polarization curves. (d) Chronoamperometric responses of Fe@Fe-SAC at 1.6 V in 1 M KOH solution.

3. Materials and Methods

3.1. Reagents and Materials

Ferric nitrate (Fe(NO₃)₃·9H₂O) was purchased from Aladdin (Shanghai, China). Sodium alginate, potassium hydroxide (KOH), and ethanol absolute (C₂H₅OH) were purchased from Sinopharm Chemical Reagent Co. Ltd. (Shanghai, China). Commercial Pt/C (20 wt.%) and IrO₂ were purchased from Alfar Aesar (Heysham, UK). Nafion solution (5 wt.% in a mixture of lower aliphatic alcohols and water) was purchased from Sigma-Aldrich (City of Saint Louis, MO, USA). The deionized water used in the experiment was obtained by secondary distillation.

3.2. Materials Synthesis

15 g of sodium alginate was dissolved in 985 mL of deionized water to form a sodium alginate sol. 20.12 g of Fe(NO₃)₃·9H₂O was added to 500 mL of deionized water to form a homogeneous aqueous solution. The 200 mL of sodium alginate sol was then added dropwise to the ferric nitrate solution. Sodium alginate cross-link with iron ions to form hydrogels. After the cross-linking reaction was complete, the hydrogel was collected from the solution. The hydrogels were freeze-dried for 48 h to completely remove water. Next, the obtained aerogels were carbonized at 700 °C under an NH₃ atmosphere for 1 h with a heating rate of 5 °C min⁻¹ and naturally cooled to room temperature.

3.3. Materials Characterization

SEM images were taken on a scanning electron microscope (MIRA3, Brno, Czech Republic). TEM images were acquired on a field emission TEM (FEI Talos F200X, Waltham, MA, USA). Atomic resolution HAADF-STEM image was characterized using a JEOL ARM200F (Tokyo, Japan) (200 kV) equipped with a cold field emission gun. X-ray diffraction was conducted on an X-ray diffractometer (Rigaku D/max-2550VL/PC, Tokyo, Japan) from 10° to 90° with a scan rate of 5° min⁻¹. Raman spectra were recorded by a Dispersive Raman Microscope (Senterra R200-L, Karlsruhe, Germany). Nitrogen adsorption–desorption measurement was conducted on a nitrogen adsorption–desorption analyzer (Quantachrome Autosorb iQ2, Boynton Beach, FL, USA) at 77.4 K. The specific surface areas were calculated based on the BET method, while the pore size distributions were calculated based on the DFT method with QSDFT adsorption model. XPS measurements were taken at a Kratos AXIS Ultra^{DL}D spectrometer (Kyoto, Japan). The binding energies of all elements were calibrated according to the C 1s peak of adventitious carbon (the binding energy of C 1s used for calibration was 284.8 eV). The spectra deconvolution was performed with the CasaXPS program (version 2.3.16, Casa Software Ltd., Teignmouth, UK) with gaussian functions after subtraction of a Shirley background.

3.4. Electrochemical Measurement

Typically, 5 mg of non-noble metal catalysts (1 mg for commercial Pt/C or IrO₂ catalyst) were dispersed in a mixture solution of 0.4 mL of ethanol, 0.6 mL of water, and 20 µL of Nafion solution, followed by ultrasonication for 1 h to obtain homogeneous ink. Next, 10 µL of the obtained catalyst ink was deposited on a glassy carbon electrode and dried at the ambient condition to form a uniform film.

ORR and OER tests were performed by a three-electrode system using a Bio-logic VMP3 electrochemical workstation at room temperature (Grenoble, France). An RDE with a diameter of 5 mm (corresponding to a geometric surface area of 0.196 cm²) was used as the working electrode, a platinum wire was used as the counter electrode, and a mercury/mercuric oxide electrode was used as the reference electrode, respectively.

For ORR tests, O₂ was passed through the electrolyte for 30 min to saturate the electrolyte with O₂. LSV curves were recorded between 0.1 V and 1.1 V versus RHE at a scan rate of 10 mV s⁻¹ with a rotation speed of 1600 rpm in 0.1 M KOH solution. For OER tests, LSV curves were recorded between 1.2 V and 1.8 V versus RHE at a scan rate of 2 mV s⁻¹ in 1 M KOH solution. The ADT for ORR was performed between 0.6 V and 1.0 V vs. RHE with a sweep rate of 100 mV s⁻¹ at room temperature. Chronoamperometric responses for OER were recorded at 1.6 V vs. RHE in 1 M KOH solution. The kinetic current density was calculated by the Koutechy–Levich equation [32]:

$$\frac{1}{j} = \frac{1}{j_K} + \frac{1}{j_L} = \frac{1}{j_K} + \frac{1}{0.2nFAC_0D_0^{2/3}\nu^{-1/6}\omega^{-1/2}} \quad (1)$$

where j is the measured current density, j_L is the diffusion-limited current density, j_K is the kinetic current density, n is the electron transfer number, F is the Faraday constant, A is the electrode's area, C_0 is the concentration of dissolved O₂ in 0.1 M KOH solution, D_0 is the diffusion coefficient of O₂, ν is the kinetic viscosity of the solution, and ω is the rotation speed of the electrode.

For RRDE tests, a rotating ring-disk electrode with a glassy carbon disk with an outer diameter of 5.61 mm and a platinum ring with an inner diameter of 6.25 mm and an outer diameter of 7.92 mm was used as the working electrode. The electron transfer number (n) and peroxide yield (H₂O₂%) can be calculated by the following two equations [33]:

$$n = 4 \times \frac{I_D}{(I_R/N) + I_D} \quad (2)$$

$$\text{H}_2\text{O}_2(\%) = 200 \times \frac{I_R/N}{(I_R/N) + I_D} \quad (3)$$

where I_D is the disk current, I_R is the ring current, and N is the ring collection efficiency.

4. Conclusions

In summary, we have developed a green and facile approach for the scalable fabrication of efficient bifunctional oxygen electrocatalysts of Fe@Fe-SAC composites. Iron nanoparticles and single atoms are uniformly distributed on the porous carbon substrates with a narrow size distribution. Fe@Fe-SAC exhibits a half-wave potential of 0.805 V for ORR, and it is stable in 10,000 potential cycles. It requires an overpotential of only 348 mV at a current density of 10 mA cm⁻² for OER in a basic electrolyte. The strong electronic interaction between nanoparticles and single atoms, hierarchical porous structure, and the graphitized carbon's physical shielding effect should be responsible for the good ORR and OER activity and stability. This work presents an efficient non-precious metal-based bifunctional oxygen electrocatalyst, promising mass production prospects and practical application.

Author Contributions: Conceptualization, B.L., F.S. and Q.L.; methodology, B.L. and F.S.; validation, S.W.; formal analysis, B.L.; investigation, B.L. and S.W.; resources, F.S. and Q.L.; data curation, B.L.; writing—original draft preparation, B.L.; writing—review and editing, B.L., S.W., F.S. and Q.L.; supervision, F.S. and Q.L.; project administration, F.S. and Q.L.; funding acquisition, F.S. and Q.L. All authors have read and agreed to the published version of the manuscript.

Funding: This research was funded by the National Natural Science Foundation of China (Grant Nos. 52072241, 51902200, and 51772187), the National High-Level Talent Program for Young Scholars, the Shanghai Science and Technology Committee (Grant Nos. 18JC1410500, 19ZR1425300 and 19ZR1425100), the Start-up Fund (F.S.) from Shanghai Jiao Tong University.

Institutional Review Board Statement: Not applicable.

Informed Consent Statement: Not applicable.

Data Availability Statement: The data supporting the reported results in this study are available upon request from the corresponding author.

Acknowledgments: We acknowledge SJTU Instrument Analysis Center for the measurements. We thank Ashkan Bahadoran for checking language errors. Bowen Liu thanks Yuanman Ni, Lingling Wu, and Qu Jiang for their help in the OER tests.

Conflicts of Interest: The authors declare no conflict of interest.

References

1. Shih, C.F.; Zhang, T.; Li, J.; Bai, C. Powering the future with liquid sunshine. *Joule* **2018**, *2*, 1925–1949. [[CrossRef](#)]
2. Chu, S.; Cui, Y.; Liu, N. The path towards sustainable energy. *Nat. Mater.* **2017**, *16*, 16–22. [[CrossRef](#)]
3. Wang, H.F.; Xu, Q. Materials design for rechargeable metal-air batteries. *Matter* **2019**, *1*, 565–595. [[CrossRef](#)]
4. Peng, L.; Shang, L.; Zhang, T.; Waterhouse, G.I. Recent Advances in the Development of Single-Atom Catalysts for Oxygen Electrocatalysis and Zinc-Air Batteries. *Adv. Energy Mater.* **2020**, *10*, 2003018. [[CrossRef](#)]
5. Wang, H.F.; Tang, C.; Zhang, Q. A review of precious-metal-free bifunctional oxygen electrocatalysts: Rational design and applications in Zn-air batteries. *Adv. Funct. Mater.* **2018**, *28*, 1803329. [[CrossRef](#)]
6. Kulkarni, A.; Siahrostami, S.; Patel, A.; Nørskov, J.K. Understanding catalytic activity trends in the oxygen reduction reaction. *Chem. Rev.* **2018**, *118*, 2302–2312. [[CrossRef](#)]
7. Lu, X.F.; Xia, B.Y.; Zang, S.Q.; Lou, X.W. Metal-organic frameworks based electrocatalysts for the oxygen reduction reaction. *Angew. Chem. Int. Ed.* **2020**, *132*, 4662–4678. [[CrossRef](#)]
8. Liu, H.; Guan, J.; Yang, S.; Yu, Y.; Shao, R.; Zhang, Z.; Dou, M.; Wang, F.; Xu, Q. Metal-Organic-Framework-Derived Co₂P Nanoparticle/Multi-Doped Porous Carbon as a Trifunctional Electrocatalyst. *Adv. Mater.* **2020**, *32*, 2003649. [[CrossRef](#)]
9. Debe, M.K. Electrocatalyst approaches and challenges for automotive fuel cells. *Nature* **2012**, *486*, 43–51. [[CrossRef](#)]
10. Li, S.; Gao, Y.; Li, N.; Ge, L.; Bu, X.; Feng, P. Transition metal-based bimetallic MOFs and MOF-derived catalysts for electrochemical oxygen evolution reaction. *Energy Environ. Sci.* **2021**, *14*, 1897–1927. [[CrossRef](#)]
11. Xia, W.; Mahmood, A.; Liang, Z.; Zou, R.; Guo, S. Earth-abundant nanomaterials for oxygen reduction. *Angew. Chem. Int. Ed.* **2016**, *55*, 2650–2676. [[CrossRef](#)]

12. Meng, F.L.; Wang, Z.L.; Zhong, H.X.; Wang, J.; Yan, J.M.; Zhang, X.B. Reactive multifunctional template-induced preparation of Fe-N-doped mesoporous carbon microspheres towards highly efficient electrocatalysts for oxygen reduction. *Adv. Mater.* **2016**, *28*, 7948–7955. [[CrossRef](#)]
13. Chen, Y.; Ji, S.; Wang, Y.; Dong, J.; Chen, W.; Li, Z.; Shen, R.; Zheng, L.; Zhuang, Z.; Wang, D.; et al. Isolated single iron atoms anchored on N-doped porous carbon as an efficient electrocatalyst for the oxygen reduction reaction. *Angew. Chem., Int. Ed.* **2017**, *129*, 7041–7045. [[CrossRef](#)]
14. Yang, F.; Xie, J.; Liu, X.; Zeng, Y.; Chen, M.; Lu, X. Iron-based nanoparticles encapsulated in super-large 3D carbon nanotube networks as a bifunctional catalyst for ultrastable rechargeable zinc–air batteries. *J. Mater. Chem. A* **2020**, *8*, 25913–25918. [[CrossRef](#)]
15. Jin, S. Are metal chalcogenides, nitrides, and phosphides oxygen evolution catalysts or bifunctional catalysts? *ACS Energy Lett.* **2017**, *2*, 1937–1938. [[CrossRef](#)]
16. Zhong, L.; Jiang, C.; Zheng, M.; Peng, X.; Liu, T.; Xi, S.; Chi, X.; Zhang, Q.; Gu, L.; Zhang, S.; et al. Wood Carbon Based Single-Atom Catalyst for Rechargeable Zn–Air Batteries. *ACS Energy Lett.* **2021**, *6*, 3624–3633. [[CrossRef](#)]
17. Zhang, J.; Chen, J.; Luo, Y.; Chen, Y.; Luo, Y.; Zhang, C.; Xue, Y.; Liu, H.; Wang, G.; Wang, R. A defect-driven atomically dispersed Fe–N–C electrocatalyst for bifunctional oxygen electrocatalytic activity in Zn–air batteries. *J. Mater. Chem. A* **2021**, *9*, 5556–5565. [[CrossRef](#)]
18. Wang, Y.; Wang, D.; Li, Y. Rational Design of Single-Atom Site Electrocatalysts: From Theoretical Understandings to Practical Applications. *Adv. Mater.* **2021**, *33*, 2008151. [[CrossRef](#)]
19. Gao, J.; Yang, H.; Huang, X.; Hung, S.F.; Cai, W.; Jia, C.; Miao, S.; Chen, H.M.; Yang, X.; Huang, Y.; et al. Enabling direct H₂O₂ production in acidic media through rational design of transition metal single atom catalyst. *Chem* **2020**, *6*, 658–674. [[CrossRef](#)]
20. Yin, S.H.; Yang, J.; Han, Y.; Li, G.; Wan, L.Y.; Chen, Y.H.; Chen, C.; Qu, X.M.; Jiang, Y.X.; Sun, S.G. Construction of highly active metal-containing nanoparticles and FeCo–N₄ composite sites for the acidic oxygen reduction reaction. *Angew. Chem., Int. Ed.* **2020**, *132*, 22160–22163. [[CrossRef](#)]
21. Yang, C.; Shang, S.; Gu, Q.; Shang, J.; Li, X.Y. Metal-organic framework-derived carbon nanotubes with multi-active Fe–N/Fe sites as a bifunctional electrocatalyst for zinc–air battery. *J. Energy Chem.* **2022**, *66*, 306–313. [[CrossRef](#)]
22. Qiao, Z.; Wang, C.; Li, C.; Zeng, Y.; Hwang, S.; Li, B.; Karakalos, S.; Park, J.; Kropf, A.J.; Wegener, E.C.; et al. Atomically dispersed single iron sites for promoting Pt and Pt₃Co fuel cell catalysts: Performance and durability improvements. *Energy Environ. Sci.* **2021**, *14*, 4948–4960. [[CrossRef](#)]
23. Shi, C.; Liu, Y.; Qi, R.; Li, J.; Zhu, J.; Yu, R.; Li, S.; Hong, X.; Wu, J.; Xi, S.; et al. Hierarchical N-doped carbon spheres anchored with cobalt nanocrystals and single atoms for oxygen reduction reaction. *Nano Energy* **2021**, *87*, 106153. [[CrossRef](#)]
24. Wang, Z.; Zhu, C.; Tan, H.; Liu, J.; Xu, L.; Zhang, Y.; Liu, Y.; Zou, X.; Liu, Z.; Lu, X. Understanding the synergistic effects of cobalt single atoms and small nanoparticles: Enhancing oxygen reduction reaction catalytic activity and stability for zinc–air batteries. *Adv. Funct. Mater.* **2021**, *31*, 2104735. [[CrossRef](#)]
25. Yang, L.; Zeng, X.; Wang, W.; Cao, D. Recent progress in MOF-derived, heteroatom-doped porous carbons as highly efficient electrocatalysts for oxygen reduction reaction in fuel cells. *Adv. Funct. Mater.* **2018**, *28*, 1704537. [[CrossRef](#)]
26. Liu, J.; Zhu, D.; Guo, C.; Vasileff, A.; Qiao, S.Z. Design strategies toward advanced MOF-derived electrocatalysts for energy-conversion reactions. *Adv. Energy Mater.* **2017**, *7*, 1700518. [[CrossRef](#)]
27. Wu, H.B.; Lou, X.W. Metal-organic frameworks and their derived materials for electrochemical energy storage and conversion: Promises and challenges. *Sci. Adv.* **2017**, *3*, 9252. [[CrossRef](#)]
28. Kou, Z.; Guo, B.; He, D.; Zhang, J.; Mu, S. Transforming two-dimensional boron carbide into boron and chlorine dual-doped carbon nanotubes by chlorination for efficient oxygen reduction. *ACS Energy Lett.* **2017**, *3*, 184–190. [[CrossRef](#)]
29. Huang, X.; Shen, T.; Zhang, T.; Qiu, H.; Gu, X.; Ali, Z.; Hou, Y. Efficient oxygen reduction catalysts of porous carbon nanostructures decorated with transition metal species. *Adv. Energy Mater.* **2020**, *10*, 1900375. [[CrossRef](#)]
30. Kang, D.; Liu, Q.; Chen, M.; Gu, J.; Zhang, D. Spontaneous cross-linking for fabrication of nanohybrids embedded with size-controllable particles. *ACS Nano* **2016**, *10*, 889–898. [[CrossRef](#)]
31. Deng, D.; Yu, L.; Chen, X.; Wang, G.; Jin, L.; Pan, X.; Deng, J.; Sun, G.; Bao, X. Iron encapsulated within pod-like carbon nanotubes for oxygen reduction reaction. *Angew. Chem., Int. Ed.* **2013**, *125*, 389–393. [[CrossRef](#)]
32. Shao, M.; Chang, Q.; Dodelet, J.P.; Chenitz, R. Recent advances in electrocatalysts for oxygen reduction reaction. *Chem. Rev.* **2016**, *116*, 3594–3657. [[CrossRef](#)]
33. Chong, L.; Wen, J.; Kubal, J.; Sen, F.G.; Zou, J.; Greeley, J.; Chan, M.; Barkholtz, H.; Ding, W.; Liu, D.J. Ultralow-loading platinum-cobalt fuel cell catalysts derived from imidazolate frameworks. *Science* **2018**, *362*, 1276–1281. [[CrossRef](#)]